

Defect migration in crystalline silicon

Lindsey J. Munro and David J. Wales

University Chemical Laboratory, Lensfield Road, Cambridge CB2 1EW, United Kingdom

(Received 1 October 1998)

A number of vacancy and interstitial defect migration mechanisms are characterized for crystalline silicon using supercells containing 64 and 216 atoms and a tight-binding approach. We investigate various defect configurations corresponding to minima and the pathways that connect them. A modified eigenvector-following approach is used to locate true transition states. We exploit the fact that only one Hessian eigenvector is needed to define the uphill search direction and use conjugate gradient minimization in the tangent space to produce a hybrid algorithm. Two implementations of this approach are considered, the first where second derivatives are available but full diagonalization of the Hessian would be the most time-consuming step, and the second where only first derivatives of the energy are known. [S0163-1829(99)02906-9]

I. INTRODUCTION

Experiments on silicon indicate that point defects may enhance dopant diffusion rates and thus affect the overall performance of silicon-based semiconductor devices. For example, it is known that supersaturation of point defects may occur during ion implantation of dopants into silicon.¹ After annealing the system at high temperature, the dopant diffusion rate is anomalously high. This is a transient effect, which depends on the intrinsic carrier concentration at the annealing temperature.² It can alter the junction depth in semiconductor devices and thus potentially degrade their performance. Electron paramagnetic resonance experiments have been interpreted in terms of mobile interstitial atoms.^{3,4} An *ab initio* investigation into the latter process suggests that silicon interstitials can have more than one charge state and that different migration barriers, and possibly different minimum energy positions, exist.⁵

There is, however, still a degree of controversy over the relative contributions of vacancies and interstitial atoms to self-diffusion and dopant diffusion.¹ Theory has made more significant progress in resolving this issue than experiments, both through *ab initio* calculations, such as those based on the local-density approximation (LDA),⁶⁻⁸ or more empirical descriptions of the energy.⁹⁻¹¹ However, fundamental properties such as defect migration pathways and diffusivities are still not well established.

Ab initio calculations are able to model defects more accurately than empirical potentials, but are limited by the high computational demands. Clark and Ackland found that defect formation energies calculated with a 64-atom cell were within 0.02 eV of the values for a 216 cell.⁸ However, extensive tests have not been completed with *ab initio* methods to check whether a 64-atom cell is large enough to ensure convergence of defect formation and migration energies. Clark and Ackland allowed for full relaxation without symmetry constraints. In some previous studies only first- and second-nearest-neighbors were allowed to relax or the symmetry around a defect was fixed.^{6,10} These restrictions both limit the validity of such studies and can affect the electrical characteristics of the defect.¹²

Empirical potentials are far less computationally demand-

ing and calculations have been carried out on an 800-atom periodic cell with full relaxation of all atoms.¹³ The usefulness of results obtained using such potentials depends on whether it is sufficient to describe the overall structure of the crystal lattice well but represent the local atomic bonding less accurately. Since no single empirical potential is clearly superior to all the others, many studies have used the Stillinger-Weber (SW) form since its successes and failures are well documented. The SW potential gives a good prediction of the melting temperature of silicon compared with experiment,¹⁴ but a poorer description of the structure of liquid silicon compared with that found using a tight-binding (TB) potential.¹⁵ An empirical potential has been developed recently that gives a better description of the local coordination and improved transferability over the SW potential.¹⁶ It has been used to study tetrahedral, hexagonal, and vacancy defects having been fitted to the unrelaxed ideal configurations. This new potential seems to be particularly successful in describing disordered structures and long-range defects, such as dislocations.

The TB approximation represents a compromise between the *ab initio* and empirical approaches since it explicitly includes the quantum-mechanical nature of the chemical bond but is also far less computationally demanding than *ab initio* calculations, typically by two to three orders of magnitude. Conversely, tight-binding theory is *slower*, by the same order of magnitude, than empirical methods with analytic potentials, but the angular nature of the bonding is correctly described far from equilibrium structures.

The structure and bonding of a system containing defects may be rather different from a regular lattice, which could invalidate empirical results. Indeed it may cause problems for the TB parametrization scheme. However, the computational efficiency of TB potentials allows us to use a periodic cell containing 216 atoms, which should be large enough to ensure that the results are converged even if we restrict \mathbf{k} -point sampling to the Γ point ($\mathbf{k}=0$). It has been argued that the practice of Γ -point sampling in a simulation cell containing only 64 atoms does not converge the forces on the atoms sufficiently to give reliable defect structures.⁸ In fact, Γ -point sampling for an eight- or nine-atom cell gives a negative formation energy.⁸ However, a previous calculation

of defect formation energies¹⁷ using the Goodwin-Skinner-Pettifor TB potential showed little difference between 512- and 216-atom cells. This finding is consistent with another study in which four different cells were used including 64, 144, 192, and 216 atoms.¹⁸ In addition, Puska *et al.* have recently provided a systematic convergence study of the silicon vacancy that suggests that Γ -point sampling for a 216-atom cell should be reasonably accurate.¹⁹ We therefore did not conduct any further tests with different \mathbf{k} -sampling schemes in the present work.

To locate transition states we have used a modified eigenvector-following (EF) approach.^{20–26} In this method we avoid some of the computational overhead involved in calculating second derivatives of the energy and diagonalizing the Hessian matrix. We have exploited the fact that only one Hessian eigenvector and eigenvalue are needed to walk uphill. An alternative fast minimization scheme such as conjugate gradient may be used in all the other directions. We have developed a hybrid eigenvector-following/conjugate gradient (EF/CG) algorithm that calculates this eigenvector and thus eliminates the need to diagonalize the Hessian. A second hybrid scheme (CG/CG) employs the same optimization procedure but does not require second derivatives and instead uses a variational theory to calculate the smallest eigenvalue and eigenvector.

In the present contribution we examine the relative performance of the hybrid optimization techniques by studying potential energy surfaces described by empirical potentials. We then apply the CG/CG technique to investigate seven different types of defects in crystalline silicon, using a non-orthogonal TB potential proposed by Menon and Subbaswamy.²⁷ We consider two different periodic cells, the first containing 64 atoms and the second 216, and use the minimum image convention to ensure that each atom interacts with the closest image of each of its neighbors. All atoms were allowed to relax. We have calculated the closest potential energy minima to certain idealized starting configurations along with the corresponding defect formation energies. Searches for transition states and the corresponding pathways were then started both from these minima and from the idealized defect configurations.

II. OPTIMIZATION TECHNIQUES

A. Eigenvector following (EF)

Details of our previous implementation of the eigenvector-following approach have been given before.^{28,29} Briefly, the method is based upon a local quadratic approximation to the potential energy surface (PES), and therefore involves first and second derivatives of the energy. An appropriate choice of Lagrange multipliers enables one to systematically maximize the energy in one direction while simultaneously minimizing in all other directions. True transition states, with a single negative Hessian eigenvalue,³⁰ can be found in this way, and minima can be located by minimizing in all directions.

B. The eigenvector-following/conjugate gradient approach

For simple empirical potentials, analytical second derivatives of the potential are often computationally inexpensive

and the rate-determining step in calculations using the eigenvector-following technique is diagonalizing the Hessian matrix. However, it is possible to use an iterative method³¹ to find the largest eigenvalue of a symmetric matrix, such as the Hessian. By a standard shifting technique we can then find the smallest eigenvalue and associated eigenvector, thus avoiding diagonalization. In the present subsection we therefore consider the case where a second derivative matrix, or Hessian, is available, but full diagonalization is undesirable.

We know that the eigenvectors \mathbf{e}_i of a symmetric matrix can be chosen to be mutually orthogonal with eigenvalues λ_i satisfying the equation

$$\mathbf{H}\mathbf{e}_i = \lambda_i \mathbf{e}_i. \quad (1)$$

Therefore, we can express an arbitrary vector \mathbf{y} as a linear combination of the \mathbf{e}_i :

$$\mathbf{y} = \sum_i a_i \mathbf{e}_i, \quad (2)$$

where a_i are the scalar coefficients. For an arbitrary vector \mathbf{y} we therefore obtain

$$\mathbf{y}_n = \mathbf{H}^n \mathbf{y} = \lambda_1^n \left[a_1 \mathbf{e}_1 + \left(\frac{\lambda_2}{\lambda_1} \right)^n a_2 \mathbf{e}_2 + \left(\frac{\lambda_3}{\lambda_1} \right)^n a_3 \mathbf{e}_3 + \dots \right]. \quad (3)$$

In the limit of large n , the term which dominates is

$$\mathbf{y}_n = \lambda_1^n a_1 \mathbf{e}_1, \quad (4)$$

where λ_1 is the eigenvalue with the largest magnitude. Repeated premultiplication of an arbitrary vector by the Hessian will generally cause that vector to become the eigenvector associated with the largest Hessian eigenvalue, in absolute terms. Normalizing the length of \mathbf{y}_n to unity at each iteration prevents it from growing too large.

The convergence of the above algorithm may be speeded up by using a shifting technique.³¹ The eigenvalues of any matrix may all be shifted by the same arbitrary value, s , without changing the eigenvectors:

$$\mathbf{H}\mathbf{e}_i = \lambda_i \mathbf{e}_i = (\lambda_i - s) \mathbf{e}_i + s \mathbf{e}_i. \quad (5)$$

Equation (5) is simply a rearrangement of the eigenvalue equation

$$(\mathbf{H} - s\mathbf{I})\mathbf{e}_i = (\lambda_i - s) \mathbf{e}_i. \quad (6)$$

Therefore, it is possible to shift the eigenvalues of the Hessian matrix at any time to reduce the fractions λ_k/λ_1 further towards zero and thus improve convergence.

If the largest eigenvalue is positive, the shifting method may then be utilized to find the smallest eigenvalue λ_{\min} by shifting all the eigenvalues down by λ_1 . At this point, the largest negative eigenvalue has the largest absolute value and we may iterate the shifted matrix as before to find it.

In the eigenvector-following/conjugate-gradient (EF/CG) hybrid approach, we use iteration and shifting to find the value of the smallest eigenvalue and the corresponding eigenvector that we intend to follow uphill. We then utilize our previous eigenvector-following formulation to calculate the size of the uphill step.^{28,29}

$$h = \frac{2F}{|\lambda_{\min}|(1 + \sqrt{1 + 4F^2/\lambda_{\min}^2})}, \quad (7)$$

where F is the component of the gradient along the eigenvector corresponding to the smallest eigenvalue \mathbf{e}_{\min} . A maximum step size, typically of 0.1 Å, was imposed for this EF step. The Polak-Ribiere conjugate gradient (CG) method³² was used to minimize the energy in the tangent space. Here we simply apply the projector $\hat{P}_{\mathbf{x}} = \mathbf{x} - (\mathbf{x} \cdot \hat{\mathbf{e}}_{\min})\hat{\mathbf{e}}_{\min}$ to all gradients throughout the CG optimization. The unit vector $\hat{\mathbf{e}}_{\min}$ is then updated and the sequence of steps is repeated until various convergence criteria are satisfied. It is only important to fully converge the CG minimization near to the desired transition state, and so a maximum of around ten CG steps was allowed. After the first cycle the eigenvectors found in the previous step can be used as input to the iterative procedure, which speeds up the process considerably. Unit vectors with randomly chosen components were used to initiate the algorithm. For each transition state the converged eigenvector corresponding to the unique negative eigenvalue was saved for use in subsequent pathway calculations. The convergence criteria employed for the TB calculations were $\lambda_{\min} < 0$, $h < 0.00001$ Å and total root-mean-square gradient < 0.00001 eV/Å.

Implementation of the above algorithm is complicated by the presence of zero or near-zero Hessian eigenvalues. In supercell calculations three Hessian eigenvalues vanish at any point because of translational symmetry. For a molecule in field-free space there are six zero eigenvalues at any stationary point, corresponding to overall translation and rotation. At a nonstationary point the rotational modes couple with vibrations to produce, typically, three normal modes corresponding to numerically small Hessian eigenvalues. In full EF calculations we project out these degrees of freedom following Baker and Hehre.³³ A projection matrix \mathbf{P} is constructed as described by Page and McIver³⁴ and applied to both the Hessian and the gradient. The projection of the Hessian to give \mathbf{PHP} would scale just as unfavorably with system size as the full diagonalization that we seek to avoid. For the same reason we do not consider any nonlinear coordinate transformations in the present work. However, in the iterative refinement of eigenvectors we can simply apply the three matrices to a given vector one after the other: there is no need to calculate the matrix product itself.

C. The conjugate-gradient/conjugate-gradient approach

The second hybrid scheme we have developed (CG/CG) uses a variational theory to find the smallest eigenvalue and corresponding eigenvector, without calculating the Hessian matrix at all. It is related to the technique proposed by Voter for accelerating molecular dynamics simulations of rare events in solids.³⁵

Consider taking a step in an arbitrary direction \mathbf{y} . We can define an ‘‘expectation value’’ for \mathbf{y} as

$$\lambda(\mathbf{y}) = \frac{\mathbf{y}^t \mathbf{H} \mathbf{y}}{\mathbf{y}^2}, \quad (8)$$

where superscript t denotes the transpose. If we define \mathbf{y} in terms of the unknown Hessian eigenvectors \mathbf{e}_i as in Eq. (2), $\mathbf{y} = \sum_i a_i \mathbf{e}_i$, and recall that the eigenvalues of these mutually orthogonal eigenvectors are λ_i , then we find a lower bound for $\lambda(\mathbf{y})$:

$$\lambda(\mathbf{y}) = \frac{\sum_i a_i^2 (\lambda_i - \lambda_{\min})}{\sum_j a_j^2} + \lambda_{\min} \geq \lambda_{\min}. \quad (9)$$

By differentiating this expression with respect to a_α , we obtain

$$\frac{\partial \lambda}{\partial a_\alpha} = \frac{2a_\alpha}{\sum_j a_j^2} \left(\lambda_\alpha - \frac{\sum_i a_i^2 \lambda_i}{\sum_j a_j^2} \right). \quad (10)$$

Setting this derivative equal to zero, we find that a possible solution is $a_\alpha = 0$, for all $\alpha \neq \min$, with a_{\min} determined by normalization. Therefore, if we minimize the value of $\lambda(\mathbf{y})$ with respect to \mathbf{y} it becomes the smallest eigenvalue of \mathbf{H} while \mathbf{y} becomes the corresponding eigenvector.

We use the numerical second derivative of the energy as an approximation to $\lambda(\mathbf{y})$, with $E(\mathbf{x}_0)$ the energy at point \mathbf{x}_0 in nuclear configuration space and $\xi \ll 1$:

$$\lambda(\mathbf{y}) \approx \frac{E(\mathbf{x}_0 + \xi \mathbf{y}) + E(\mathbf{x}_0 - \xi \mathbf{y}) - 2E(\mathbf{x}_0)}{(\xi \mathbf{y})^2}, \quad (11)$$

and use conjugate gradient minimization to find the required minimum. If we keep $|\mathbf{y}| = 1$, then differentiating Eq. (11) gives

$$\frac{\partial \lambda}{\partial \mathbf{y}} = \frac{\nabla E(\mathbf{x}_0 + \xi \mathbf{y}) - \nabla E(\mathbf{x}_0 - \xi \mathbf{y})}{\xi}. \quad (12)$$

Once the smallest eigenvalue and the corresponding eigenvector are known we can proceed to find transition states using eigenvector following for the uphill step and conjugate-gradient minimization in the tangent space, as for the EF/CG method above.

To prevent contamination of the desired eigenvector by modes corresponding to overall translation or rotation a simple projection scheme was applied both to the vector \mathbf{y} and the derivative $\partial \lambda / \partial \mathbf{y}$. Unit vectors corresponding to infinitesimal translational and rotational displacements are easily calculated.³⁴ All components of \mathbf{y} and $\partial \lambda / \partial \mathbf{y}$ in these directions were then removed by orthogonalization.

D. Pathways

We have successfully located transition states from both minima and idealized defect configurations using the above methods. Hence the new hybrid formulations preserve the highly desirable feature of eigenvector following that a good guess of the transition state geometry is not needed. Having found a transition state, we calculate the corresponding pathway by adding (or subtracting) a small fraction of the eigenvector corresponding to the unique negative Hessian eigenvalue to the transition-state coordinates. Searches for minima can then be initiated from the resulting geometries either using eigenvector-following minimization or conjugate-

gradient methods, among others. These paths are expected to be close to steepest-descent paths, although they are not strictly the same.³⁶

III. POTENTIALS EMPLOYED IN OPTIMIZATION TESTS

The simplest system we have considered is a supercell containing 257 atoms modeled by the Lennard-Jones (LJ) potential with periodic boundary conditions. We have used the minimum image convention³⁷ without a cutoff to avoid discontinuities in the energy. Hence each atom is allowed to interact with the minimum image of all the other atoms in the supercell. This procedure does not give a uniform description of the more distant interactions. However, it enabled us to overcome some technical difficulties with the geometry optimizations, and our convergence tests indicate that it does not lead to any major artifacts. The system we have studied is a face-centered-cubic (fcc) lattice with an interstitial atom inserted in it. The LJ potential energy is given by

$$E_{\text{LJ}} = 4\epsilon \sum_{i < j} \left[\left(\frac{\sigma}{r_{ij}} \right)^{12} - \left(\frac{\sigma}{r_{ij}} \right)^6 \right], \quad (13)$$

where ϵ is the pair well depth, $2^{1/6}\sigma$ is the pair equilibrium separation, and r_{ij} is the distance between atoms i and j . The main advantage of this potential is its computational simplicity.

The next calculations were started from a 309-atom Mackay icosahedron³⁸ bound by a Morse (M) potential.³⁹ The Morse potential may be written as

$$E_{\text{M}} = \epsilon \sum_{i < j} e^{\rho_0(1-r_{ij}/r_e)} (e^{\rho_0(1-r_{ij}/r_e)} - 2), \quad (14)$$

where ϵ is the pair well depth, as before, and r_e is the pair equilibrium separation. In this study we have set $\rho_0 = 6$, where the Morse and LJ potentials have the same curvature at the bottom of the well.

Sutton and Chen (SC) based their model for fcc metals⁴⁰ on the Finnis-Sinclair potentials for body-centred-cubic metals,⁴¹ which include a many-body term:

$$E_{\text{SC}} = \epsilon \sum_i \left[\frac{1}{2} \sum_{j \neq i} \left(\frac{a}{r_{ij}} \right)^n - c \sqrt{\rho_i} \right], \quad (15)$$

where

$$\rho_i = \sum_{j \neq i} \left(\frac{a}{r_{ij}} \right)^m, \quad (16)$$

c is a dimensionless parameter and a is the lattice constant. ϵ is a parameter with dimensions of energy and is fitted to the experimental cohesive energy for each metal. m and n are positive integers with $n > m$ and $m > 6$.⁴⁰ We use the parameters given by Sutton and Chen⁴⁰ for nickel: $\epsilon = 0.015707$ eV, $c = 39.432$, $n = 9$, and $m = 6$ and studied a 500-atom fcc cell with an extra atom inserted in the lattice and periodic boundary conditions. As for the LJ potential, we have employed the minimum image convention with no cutoff.

The effects of angular forces are intrinsically included when the Hamiltonian is given in a parametrized form using a tight-binding method. We have used the transferable tight-

TABLE I. Comparison of CPU time taken (relative values) to locate a transition state for the LJ₂₅₇ periodic system. The largest and smallest eigenvalues (in ϵ/σ^2) for the starting configuration are also included. ceig is the convergence parameter for the % change in the eigenvalue in question.

Method	ceig/%	Largest eigenvalue	Smallest eigenvalue	Time
EF		12251.2	-65.747	20.8
EF/CG	0.001 ^a	12251.1	-55.551	1.2
EF/CG	0.01	12250.2	39.110	1.2
EF/CG	0.1	8927.5	-2428.419	1.0
CG/CG	0.01		-59.378	20.1
CG/CG	0.1		-57.813	48.7
CG/CG	1		-54.504	3.5

^aA tighter convergence criterion is needed to produce a good estimate of the smallest eigenvalue at the high-energy initial configuration used. The runs with ceig=0.01 and 0.1 converged to the same transition state despite relatively poor values for λ_{\min} at the starting point.

binding scheme (M&S₉₇), proposed by Menon and Subbaswamy²⁷ for silicon in both these preliminary tests of our hybrid methods and in the more comprehensive study of silicon defects that follows. This scheme incorporates the nonorthogonality between the atomic orbitals in its parametrization. It is therefore more suitable for describing systems where the bonding is not necessarily tetrahedral than earlier orthogonal schemes.^{42,43} To compare the optimization techniques we considered an interstitial atom in a cell of 64 atoms with periodic boundary conditions, minimum image convention, and no cutoff, as above.

IV. PERFORMANCE OF THE OPTIMIZATION ALGORITHMS

If we first look at the results of some transition state searches using the LJ potential in Table I, we can see there are a number of factors that can affect the reliability of the two hybrid techniques. The performance of the iterative approach (EF/CG) depends on how well the largest eigenvalue, found first, is converged, particularly at the starting configuration. We found that in order to ensure successful convergence to a transition state, the percentage difference between successive values of the iterated eigenvalue at convergence had to be either 0.1% or 0.01%. For optimizations on systems modeled by the other potentials, the convergence criterion had to be 0.01%, and for this reason we will only consider results found using this value in our subsequent discussions. The second hybrid method based on variational theory (CG/CG) only requires the smallest eigenvalue and could therefore succeed with a less stringent convergence criterion of 1%.

The searches all converged to the same stationary points. This would not necessarily be true for arbitrary starting points, but here we have been careful to compare timings for equivalent searches. Both of the hybrid techniques find minima using the same conjugate-gradient method, so results for the CPU time taken to find these stationary points are the same in Table II.

TABLE II. CPU time taken (relative values) in searches for minima (Min), transition states (TS), and pathways (Path) for the three optimization methods discussed. The pathways and minima were calculated by conjugate-gradient minimization for both EF/CG and CG/CG, and by EF minimization for EF.

System	Technique	Time taken			Number of steps	
		Min	TS	Path	Min	TS
LJ ₂₅₇	EF	59.7	46.2	66.0	32	26
	EF/CG	2.6	2.6	3.6	125	13
	CG/CG	2.6	7.7	3.6	125	21
M ₃₀₉	EF	52.3	47.8	98.5	10	9
	EF/CG	1.0	1.3	2.0	62	8
	CG/CG	1.0	1.6	2.0	62	8
SC ₅₀₁	EF	146.6	801.7	1708.9	7	38
	EF/CG	10.2	162.7	64.1	38	20
	CG/CG	10.2	417.7	64.1	38	53
(M&S ₉₇) ₆₅	EF ^a	1531.3	1138.2	434.4	128	95
	CG/CG	75.7	165.12	141.4	61	11

^aWith numerical rather than analytical second derivatives.

The number of optimization steps taken to locate a transition state for each of the hybrid techniques is similar. Given the same eigenvalue and eigenvector to follow uphill at each step they would be identical. The EF/CG approach, which avoids diagonalizing the Hessian, is clearly the most efficient method for finding transition states in large systems when analytical second derivatives are relatively inexpensive. The greatest improvement in speed over the EF approach is by a factor of 38 for the M₃₀₉ system, for EF/CG, and a factor of 30, for CG/CG. The increase in efficiency is less impressive for SC₅₀₁ and TB₆₅, but perhaps more significant since the searches take considerably longer.

The SC₅₀₁ periodic system caused difficulties for all three methods. The smallest eigenvalue calculated using the CG/CG method was initially incorrect because of intrinsic problems with the numerical derivative caused by energy discontinuities due to the periodic boundary conditions. However, the CG/CG method did eventually find the same transition state as the other methods.

V. DEFECTS IN CRYSTALLINE SILICON

A. Characterizing the reaction pathways

Conjugate-gradient minimization was used to locate minimum-energy structures from the starting configurations. We then used EF (with numerical second derivatives) and the CG/CG hybrid technique to find transition states and pathways with a periodic cell of 64 atoms. The primary purpose of the EF calculations, which took considerably longer (see Table II), was to verify the results obtained using the new CG/CG method. These were found to be accurate and thus we only considered the hybrid method in our calculations for the larger periodic cell.

All optimizations were first carried out for the smaller periodic cell and then the stationary points were reoptimized by wrapping an extra layer of atoms around the original configurations to give a 216-atom cell. The pathways were then

recalculated from the new transition states. Hence we have checked that the formation and migration energies are well converged. Searches for minima from the idealized defect configurations in the larger periodic cell were also carried out as a further check.

The reaction pathways were characterized by calculation of several other properties. The moment ratio of displacement γ is⁴⁴

$$\gamma = \frac{N \sum_i [\mathbf{Q}_i(s) - \mathbf{Q}_i(t)]^4}{\left\{ \sum_i [\mathbf{Q}_i(s) - \mathbf{Q}_i(t)]^2 \right\}^2}, \quad (17)$$

where $\mathbf{Q}_i(s)$ is the position vector of atom i in minimum s , etc. and γ is dimensionless. If only a single atom moves then $\gamma = N$ and the rearrangement is strongly localized. Alternatively, if all of the atoms move through the same distance then $\gamma = 1$ and the process is completely cooperative, i.e., delocalized. The distance between minima in nuclear configuration space is

$$D = \sqrt{\sum_i [\mathbf{Q}_i(s) - \mathbf{Q}_i(t)]^2}. \quad (18)$$

The calculation of defect formation energies in the bulk structures employs the diamond structure for 64 or 216 particles as a reference. We rescale the energy of the defect structure so that both systems contain 64 or 216 atoms. Let N' be the number of particles in the defect structure and $E_{N'}$ the corresponding energy. Then the formation energy (E_f) for the larger supercell was estimated as

$$E_f \approx \frac{216}{N'} E_{N'} - E_{216}. \quad (19)$$

B. Starting configurations

Five idealized self-interstitial configurations were considered as starting points for diamond cubic silicon. The bond-centered interstitial is created by breaking one of the Si-Si bonds and placing an additional atom in the center, as shown by the atom at $(a/8, a/8, a/8)$ bisecting a bond along the $[111]$ direction in Fig. 1, where a is the box length of a unit cell (5.427 Å). In the dumbbell, or $\langle 100 \rangle$ -split interstitial, one Si atom of the perfect crystal located at $(a/2, a/2, 0)$ is replaced by two Si atoms at $([1/2 \pm \sqrt{3}/8]a, 0, 0)$. In the $\langle 110 \rangle$ -split interstitial the two replacement atoms are at $([1/2 \pm 0.169]a, [1/2 \pm 0.169]a, 0)$ instead of the origin.⁴⁵ Tetrahedral-site and hexagonal-site interstitials are located at $(a/2, a/2, a/2)$ and $(3a/8, 3a/8, 5a/8)$, respectively. These positions are low charge-density regions in the Si crystal.¹³ The position of each of the interstitial atoms within a conventional unit cell is illustrated in Fig. 1. We also considered a sixth interstitial site where the atom was placed on a mirror plane, at $(3a/8, -3a/8, -3a/8)$, so that the structure has C_s symmetry, and finally, a single vacancy structure. We did not search for defects containing three-membered rings^{8,51} in this study.

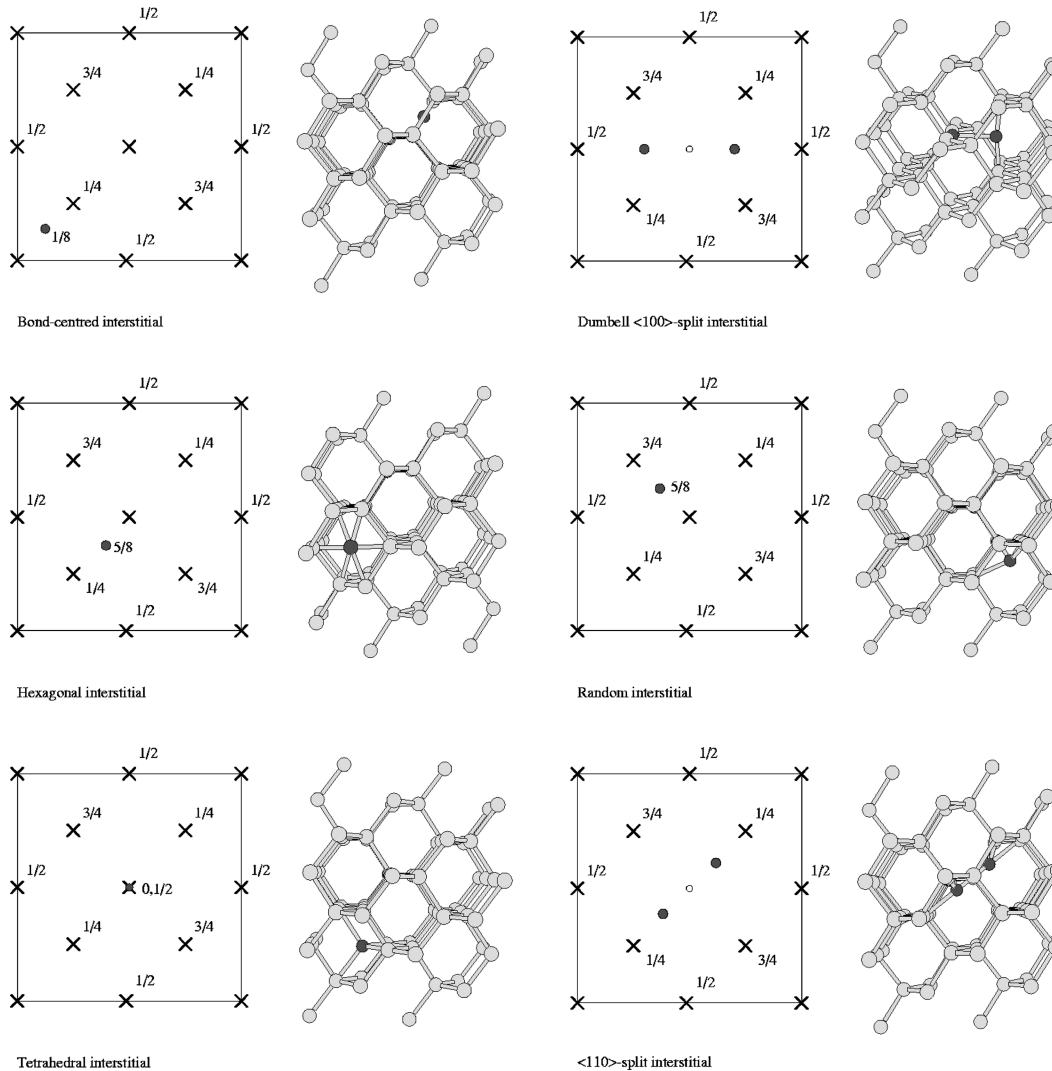


FIG. 1. Position of the six different interstitial configurations considered in the present work. Atoms marked by a cross are part of the perfect diamond lattice, while those represented by a filled circle are interstitial atoms. Vacancies are indicated by unfilled circles.

C. Problems with the conjugate-gradient optimizations

The conjugate-gradient optimizations proved to be very sensitive to any discontinuities in the energy. Small discontinuities arise if the minimum image of one atom with respect to any other shifts during the optimization. To circumvent such problems the minimum images for all pairs of atoms were not allowed to jump during conjugate gradient optimizations. A small shift in the energy may then occur at the start of the next cycle, when all the minimum images are updated. Despite this procedure a few runs still failed to converge, and we found that altering the step or pushoff size (from a transition state) did not usually help in these cases. Sometimes, both sides of a pathway led to exactly the same minimum for the 64-atom cell, but such results were artifacts of the fixed image scheme. We were only able to resolve these particularly difficult cases by moving to a larger supercell.

VI. RESULTS

A. Defect formation energies

Four interstitial minima were found from our six starting configurations, as shown in Table III. The results are quali-

tatively the same for the 64- and 216-atom periodic cells. The percentage difference between formation energies is small and shows a slight increase as a result of including interactions with more distant atoms for the larger cell size.

TABLE III. Minimum-energy configurations found from idealized starting arrangements and the formation energies (in eV) of these minima from optimizations carried out for a periodic cell containing 216 atoms, $E_f(216)$. The % difference between these energies and those found with the smaller cell size containing 64 atoms is given as ΔE . The Hessian index of the stationary point that lies closest to the initial idealized configuration is also given.

Starting configuration	Nearest minimum	$E_f(216)$	ΔE (%)	Index of nearest stationary point
Bond	$\langle 110 \rangle$	5.546	1.70	2
Dumbell	$\langle 110 \rangle$	5.546	1.70	2
Hexagonal	$\langle 110 \rangle$	5.546	1.70	2
C_s	Extended	8.103	0.72	4
Tetrahedral	Tetrahedral	8.096	0.75	2
$\langle 110 \rangle$	$\langle 110 \rangle'$	5.618	2.11	1
Vacancy	Vacancy	3.902	-4.22	0

This result is consistent with a previous study that also uses a TB potential.¹⁸ Formation of a vacancy is the most energetically favorable process. The vacancy lies at the center of a Jahn-Teller distorted (D_{2d}) tetrahedron of atoms, which are drawn in towards it by around 0.5 Å. Increasing the size of the periodic cell actually decreases the formation energy because the atoms around the defect are displaced by up to 0.05 Å less when interactions with more distant atoms are taken into account. The energies and distances quoted in the text are all from calculations with the larger periodic cell size unless stated otherwise.

The bond, dumbbell, and hexagonal interstitial arrangements all collapsed to a $\langle 110 \rangle$ -split interstitial, with atoms separated by 2.25 Å, which differs by only 0.002 Å from the result found at the smaller cell size. This $\langle 110 \rangle$ -split interstitial was the lowest-energy interstitial structure that we found. However, the minimization started from the idealized guess for the $\langle 110 \rangle$ -split interstitial found a slightly higher energy form of this defect ($\langle 110 \rangle'$), with a somewhat greater separation of 2.41 Å. The separation is 0.02 Å smaller than for the 64-atom periodic cell. The outward displacement of neighboring atoms by 0.1–0.2 Å in these $\langle 110 \rangle$ -split interstitial arrangements extends as far as 4 Å along the axis of the split interstitial and 2 Å to either side. This effect is slightly more pronounced in the higher-energy configuration.

Both the tetrahedral interstitial and the C_s starting configurations led to minima in which the interstitial atoms were in unfavorable positions. There is a slight amount of outward relaxation around the tetrahedral interstitial leading to a D_{2d} Jahn-Teller distortion of the tetrahedron surrounding this atom. The closest saddle point to the C_s starting geometry, which was determined by a modified Newton-Raphson optimization from the original geometry, was actually an index four saddle point (i.e., with four negative Hessian eigenvalues). Here we used numerical second derivatives for the smaller supercell and steps of the form

$$h_i = \frac{-2F_i}{\lambda_i(1 + \sqrt{1 + 4F_i^2/\lambda_i^2})}, \quad (20)$$

for eigendirection i . A trust radius scheme was employed for the maximum step sizes, as described elsewhere.²⁹ Near convergence $h_i \rightarrow -F_i/\lambda_i + (F_i/\lambda_i)^3$ and so the conventional Newton-Raphson step is recovered that can produce convergence to a stationary point of any Hessian index.^{46,47}

As we can see from Fig. 2, the minimum energy structure found from the C_s starting configuration is an extended interstitial arrangement that has been formed by displacing a next-nearest neighbor into a similar site in an adjacent hexagon, with a separation of 5.43 Å. We reserve the term “extended interstitial” for fully relaxed configurations with interstitial atoms separated by more than one nearest-neighbor distance.

The closest stationary points to the bond, dumbbell, and hexagonal configurations, calculated using the modified Newton-Raphson scheme, all had Hessian index two. The bond-centered interstitial was also found to have index two in a previous search to characterize the potential energy surface using the SW potential.¹¹ The latter study reported that the hexagonal interstitial lay closest to an index three saddle point. In our calculations the $\langle 110 \rangle$ -split interstitial actually

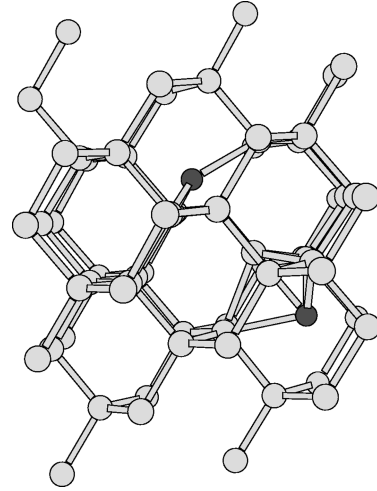


FIG. 2. Extended interstitial minimum found from an interstitial placed in a C_s site.

lies closest to a transition state configuration, which is also identified in the explicit search for a transition state in the next section. It is important to note that a considerable amount of relaxation has taken place in reaching these higher index stationary points, particularly from the bond, C_s , and $\langle 110 \rangle$ starting geometries. Therefore we cannot expect these higher index stationary points to give us any idea about the true migration pathways.

We found that searches for minima started from the original starting configurations with the larger periodic cell gave the same results as for reoptimization of the results from the smaller cell, except for the dumbbell $\langle 100 \rangle$ -split interstitial and the hexagonal interstitial arrangements. In both cases, we found a new split interstitial oriented in a $\langle 10\bar{3}3 \rangle$ direction, which we shall refer to as an A -type split interstitial. This defect has a formation energy of 6.106 eV.

Results from previous calculations with a range of potentials do not give a consistent picture, as shown in Table IV, even when comparing only *ab initio* methods or only empirical potentials. The values predicted for the defect formation energies highlight the importance of ensuring that the periodic cell is not too small. The lowest-energy structure predicted by the study of Zhu *et al.*⁴⁸ (ZDY₉₆) is a $\langle 110 \rangle$ -split interstitial for a 64-atom periodic cell. However, calculations on a smaller cell containing only 32 atoms in the same study, found that the hexagonal defect lay lower in energy. Clark and Ackland⁸ (ClarkA₉₇) also used a 64-atom periodic cell. Both of these studies using the larger cell size predict formation energies that are two to three times those found by Chadi⁴⁵ using a 32-atom cell. The table also shows the lack of any systematic studies for previous TB and *ab initio* approaches. The empirical study by Nastar *et al.* is more comprehensive.¹¹

Although there are no quantitatively accurate results to compare with, some trends do appear from these previous calculations. The $\langle 110 \rangle$ -split interstitial is generally found to be the lowest-energy interstitial configuration. In the study by Nastar *et al.*¹¹ using the empirical SW potential, the $\langle 110 \rangle$ -split interstitial becomes lower in energy than the extended interstitial configuration when the volume is expanded by 2%. These complex defects tend to be low in energy, as shown by the defect formation energy of the cage

TABLE IV. Defect formation energies (in eV) with other potentials: Nastar₉₆ (Ref. 11), LKK₉₇ [Lenosky *et al.* (Ref. 18)], TCZD₉₇ [Tang *et al.* (Ref. 53)], Chadi₉₂ (Ref. 45), ZDY₉₆ Zhu *et al.* (Ref. 48), [ClarkA₉₇ (Ref. 8)] and from the current work using the M&S₉₇ potential.

Defect	SW		TB		<i>Ab initio</i>		
	Nastar ₉₆	LKK ₉₇	TCZD ₉₇	Chadi ₉₂	ZDY ₉₆	ClarkA ₉₇	M&S ₉₇
Bond	a			1.2			b
Extended	3.91 ^c					2.29 ^d	8.10
Hexagonal	e	4.03	4.93	1.0	3.3	2.45	b
Tetrahedral	5.28	3.75	4.39				8.10
$\langle 100 \rangle$	5.59			1.8			b
$\langle 110 \rangle$	4.68		3.80	0.9	3.2	2.16	5.55
Vacancy		3.68	3.97		4.1 ^f		3.90

^aIndex two saddle point.

^bCollapses to $\langle 110 \rangle$ minimum.

^c $\langle 110 \rangle$ -split interstitial is lower in energy when the cell volume is expanded by 2%.

^dThis is a ‘‘cage’’ arrangement in which the interstitial atom is caged by 10 atoms in asymmetric positions.

^eIndex three saddle point.

^fFrom Ref. 49.

structure discovered by *ab initio* calculations.⁸ Indeed the low energy of the $\langle 110 \rangle$ -split interstitial can be linked to a spread of the interaction with the defect atoms over a larger volume, thus reducing the overall formation energy. The relative formation energies for the other defects vary greatly. One of the TB calculations predicts that the vacancy formation energy is actually the lowest, in agreement with our findings, but contrary to those of a recent *ab initio* calculation.⁴⁹

We find that the lowest interstitial formation energy is that of the $\langle 110 \rangle$ -split interstitial and that several different starting configurations all collapse to this arrangement. We also found that the tetrahedral interstitial is energetically unfavorable. The extended interstitial arrangement that we have identified extends over a greater range than either of the other two examples found in the literature and shown in Table IV. The energetics are therefore different.

B. Defect migration pathways

Searches for transition states from the five different defect minima and the seven idealized starting configurations found only four different transition states, three with interstitial atoms and one with a vacancy. These four transition states

were again found after reoptimizing with the larger periodic cell containing 216 atoms. We also searched for transition states from the reoptimized minima with the larger cell size. These calculations are far more time consuming, and the majority of the results were unchanged. However, we did find one additional transition state and pathway linking a previously uncharacterized minimum, namely, a complex defect involving three interstitial atoms and two vacancies, to an A-type split interstitial minimum. The pathways that link minima via these transition states are listed in Table V.⁵⁰

The pathway linking the lowest-energy $\langle 110 \rangle$ -split interstitial to the higher-energy split interstitial structure involves a small barrier of 0.072 eV. The barrier for the reverse process is very small, indicating that the PES is very flat in this region. The two other interstitial pathways we have found both link the $\langle 110 \rangle$ -split interstitial to an A-type split interstitial. Figure 3 illustrates the high-energy pathway that links a $\langle 110 \rangle$ -split interstitial to an A-type split interstitial via a translation. The low-energy pathway converts an A-type split interstitial to a $\langle 110 \rangle$ -split interstitial by a rotation, as shown in Fig. 4. From the migration energies given in Table V we can see that the barrier to rotation in this latter pathway is extremely small. Therefore, the two pathways could together

TABLE V. Barrier heights for both the forward and reverse defect migration pathways (ΔE_1 and ΔE_2 in eV), calculated for a periodic cell of 216 atoms. The percentage changes from the results found with the smaller periodic cell are given as %₁ and %₂. In addition, the moment ratio of displacement γ , indicating the degree of cooperativity, and D , the distance between the minima in nuclear configuration space in Å, are also given. Finally, a brief description of the pathway is included, in which nn indicates nearest neighbor.

Pathway	ΔE_1	% ₁	ΔE_2	% ₂	γ	D	Description
$\langle 110 \rangle \rightarrow \langle 110 \rangle'$	0.072	30	a	0	26.26	0.92	Stretch
$\langle 110 \rangle \rightarrow \langle 10 \ 3 \ 3 \rangle$	0.961	3	0.399	20	30.47	1.96	Translation
$\langle 110 \rangle \rightarrow \langle 10 \ 3 \ 3 \rangle$	0.596	-9	0.034	-15	43.86	1.37	Rotation
$\langle 10 \ 3 \ 3 \rangle \rightarrow$ complex	0.610		0.098		40.13	1.71	Rotation
Vacancy \rightarrow vacancy	0.632	26	0.632	26	12.26	1.56	Degenerate
Vacancy \rightarrow vacancy	0.723	16	0.723	16	56.92	2.02	nn migration

^a ΔE_2 is smaller than our convergence limit.

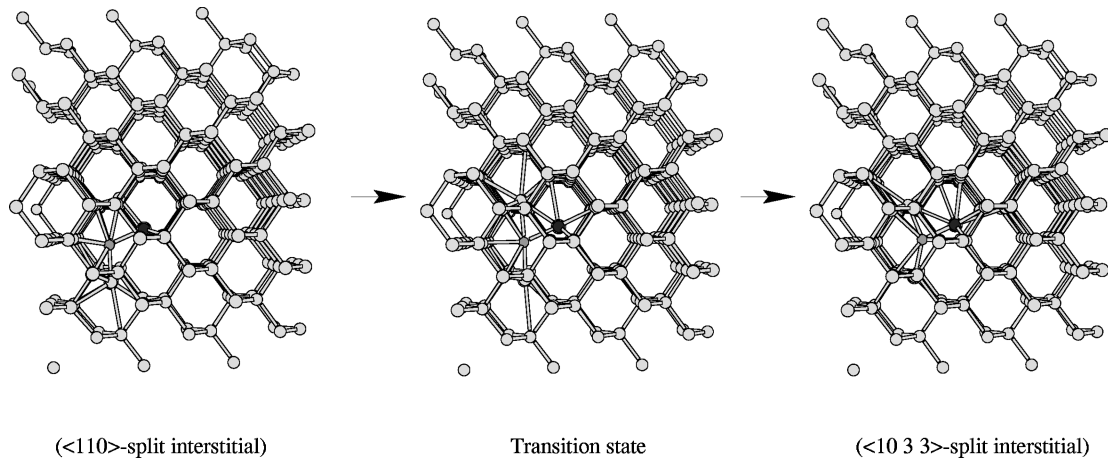


FIG. 3. Rearrangement pathway from the A-type split interstitial in a $\langle 10\bar{3}3 \rangle$ direction to a $\langle 110 \rangle$ -split interstitial via a high-energy transition state.

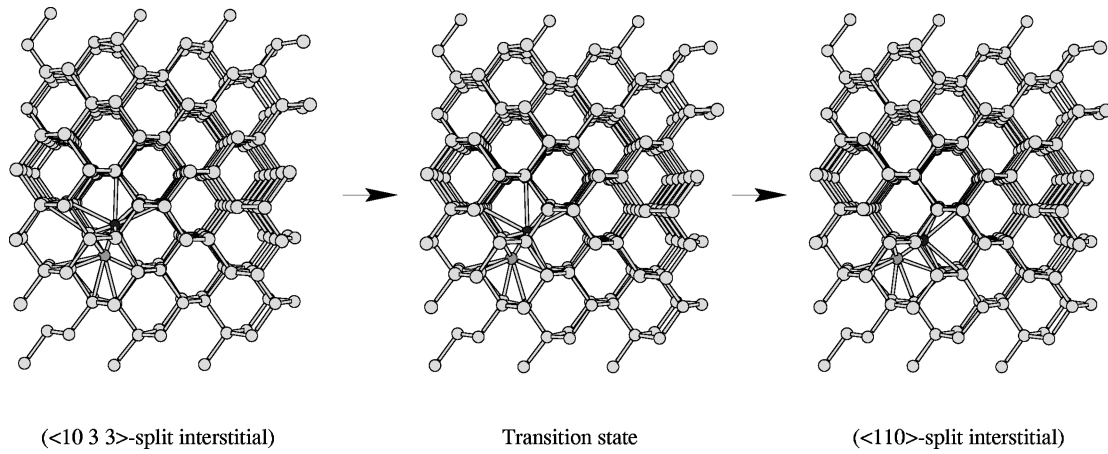


FIG. 4. Rearrangement pathway from the $\langle 110 \rangle$ -split interstitial to an A-type split interstitial in a $\langle 10\bar{3}3 \rangle$ direction via a low-energy transition state.

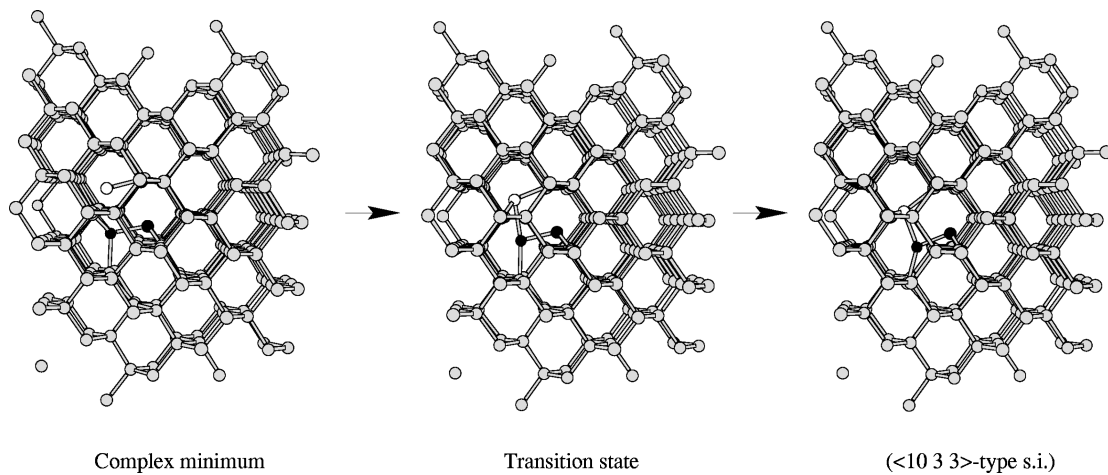


FIG. 5. Rearrangement pathway from a complex defect to an A-type split interstitial in a $\langle 10\bar{3}3 \rangle$ direction via a high-energy transition state.

provide a migration mechanism for $\langle 110 \rangle$ -type split interstitials by first translating to an A -type split interstitial in a $\langle 1033 \rangle$ direction and then rotating to a different $\langle 110 \rangle$ -split interstitial.

The A -type split interstitial is also involved in the pathway that was found in the search for a transition state from a reoptimized $\langle 110 \rangle$ -split interstitial minimum. The mechanism, shown in Fig. 5, starts from a high-energy minimum, with a defect formation energy of 6.615 eV, and can be described as a triangle of atoms around a vacancy. The second vacancy lies below the split interstitial represented by the two black atoms and is adjacent to the first. The white atom moves towards the first vacancy that displaces the other two interstitial atoms towards the second vacancy. They subsequently rotate slightly and orient themselves to give the A -type split interstitial. The barrier for the reverse process is considerably higher than that for either of the paths to convert an A -type split interstitial to a $\langle 110 \rangle$ -split interstitial and is therefore unlikely to play a significant role in the diffusion of defects.

The percentage difference between results given for pathways with 217 atoms and those obtained using a smaller periodic cell show that there are significant interactions between more distant atoms. However, the results are qualitatively unchanged. In the pathway in which the motion is primarily a translation, both atoms move through the lattice and both can interact with an increased number of atoms in surrounding shells. Therefore, the migration energy rises due to the increased number of atoms affected by the defect. The converse is true for the rotational motion, in which basically only one atom moves, decreasing the overall amount of disruption and leading to a decrease in migration energies at the larger cell size. This is reflected by the cooperativity indices for each of these pathways: the translation motion involves the displacement of more atoms, indicating a more delocalized pathway and thus γ lies closer to unity than it does in the case of the rotation mechanism.

The pathway we found involving a vacancy from our initial set of optimizations is not a migration process, but rather a degenerate rearrangement⁵² in which the tetrahedron of atoms around the vacancy rotates to an equivalent configuration. The vacancy does not move. The significant increase in the energy for this rotation calculated at the larger size is due to the slight displacement of a large proportion of the atoms in the periodic cell, as indicated by the low cooperativity index γ in Table V. We did succeed in locating a transition state for vacancy migration from a starting point close to the idealized geometry of this stationary point. In this process, the vacancy migrates to a nearest-neighbor position. The larger value of the cooperativity index confirms that this is a more localized path than the previous vacancy mechanism. The barriers for this migration pathway are of the same order as for the interstitial pathways described above. However, the activation energy is significantly lower ($E_{\text{act}}^{\text{v}} = 4.623$ eV) than that predicted for interstitial pathways [$E_{\text{act}}^{\text{i}} = 6.507$ eV (translation) or 6.142 eV (rotation)] due to the low vacancy formation energy. These results are in broad agreement with experimental estimates of E_{act} that lie in the range 4–6 eV.

From our results, we would expect vacancy diffusion to dominate at low temperature and interstitials to have more impact at high temperature. This prediction is consistent with

TABLE VI. Defect migration pathways found in previous studies. Energies are all in eV. E_m is the migration energy and E_{act} is the activation energy, which includes the defect formation energy. The potential is indicated along with the appropriate reference.

Pathway	E_m	E_{act}	Potential
$T \rightarrow H \rightarrow T$	1.0	5.0	TB (Ref. 54)
$\langle 110 \rangle \rightarrow T \rightarrow \langle 110 \rangle$	1.37	5.1	TB (Ref. 53)
$\langle 110 \rangle \rightarrow B \rightarrow \langle 110 \rangle$	0.65	5.3	SW (Ref. 11)
Ext $\rightarrow \langle 110 \rangle$	1.62	5.5	SW (Ref. 11)
Tetrahedral \rightarrow Bond		6.5	DFT (Ref. 6)
Vacancy \rightarrow Vacancy	0.3	3.5	TB (Ref. 54)
Vacancy \rightarrow Vacancy	0.1	4.2	TB (Ref. 53)

recent work by Tang *et al.*,⁵³ whose predicted crossover temperature is in good agreement with the experimental estimate of 1050 °C. However, they obtained the migration energy for vacancies, shown in Table VI, by an Arrhenius interpolation of the diffusivity data collected in molecular-dynamics (MD) simulations that cannot explicitly describe the mechanism.

We found that a variety of pathways have been suggested for the diffusion of defects in previous studies, with a wide range of predicted activation energies, as shown in Table VI. No single pathway was favored in a recent MD simulation using an *ab initio* pseudopotential approach.⁸ Migration was found to occur by excitation of a single atom, which could then travel significant distances through the open diamond structure, before being recaptured.⁸ An *ab initio* investigation into electron-assisted transport mechanisms found that electron-assisted migration occurred through the tetrahedral-hexagonal-tetrahedral path.⁵ This path involves charged Si^{2+} species and uncharged interstitial atoms, and therefore we have not included it in our table. A further drawback of that study is that the periodic cell contained only 16 atoms, which in the light of subsequent *ab initio* investigations is probably too few. The same pathway has also been found with a 216-atom cell and a TB potential,⁵⁴ but in this case the hexagonal interstitial configuration has not been characterized as the transition state. Instead, the activation energy, given in Table VI, is simply a combination of the formation energy for a tetrahedral interstitial and the difference between formation energies of the latter arrangement and a hexagonal interstitial geometry. A similar approach was used to obtain the vacancy activation energy in the same study, which is also shown in the table.

The activation energies of each of the pathways found in the second TB study⁵³ included in Table VI are simply estimates from MD calculations. In this case, only one interstitial pathway was elucidated by analysis of MD trajectories. In this pathway, as in our calculations, a $\langle 110 \rangle$ -split interstitial was seen to migrate to an adjacent site, but the results from this TB-MD study indicate that this is a one-step process, via a tetrahedral interstitial.

The DFT/LDA calculation,⁶ which predicts an activation energy of 6.5 eV for the migration of a tetrahedral interstitial to a bond-centered site, does not specify the number of atoms used in the periodic cell. The transition state has not been explicitly calculated in either this DFT calculation or the previously mentioned TB-MD study. Similarly, the first of the two mechanisms in Table VI calculated using the empiri-

cal SW potential and the discretized path method connects two $\langle 110 \rangle$ -split interstitials via an index two saddle point.¹¹ A true transition state was not located for this pathway. This result is inconsistent with the Murrell-Laidler theorem,³⁰ which states that if two minima are connected by a saddle of index two or more then they are linked by one or more saddles of index one with lower energies. The second path, found in the same study, links an extended interstitial via a true transition state to a $\langle 110 \rangle$ -split interstitial.

C. Eigenvector-following results

Our searches for defect minima and transition states using numerical second derivatives, full diagonalization and the smaller supercell, were in good agreement with our findings using the hybrid methods. Minimization of all the starting configurations led to the lowest-energy $\langle 110 \rangle$ -split interstitial minima that we had found before, except for the search started from the $\langle 100 \rangle$ -split interstitial or dumbbell configuration. In the latter case, the minimum located was the A-type split interstitial in a $\langle 10\ 3\ 3 \rangle$ direction. No new pathways or transition states were obtained.

VII. DISCUSSION

We have demonstrated the effectiveness of the CG/CG approach, which eliminates the need for a Hessian, by using it to find transition states and pathways with a periodic supercell containing 216 atoms and a TB potential for silicon.

The results from previous calculations on silicon defects indicate that the $\langle 110 \rangle$ -split interstitial is involved in low-energy pathways and are in reasonable agreement with our predicted activation energies. Our results highlight the diverse range of defects and pathways that may exist and the

need for a systematic approach to identifying pathways without any geometrical constraints. We have also investigated the dependence of migration energies, and to a lesser extent the formation energies, on the size of the supercell.

We have found that for the M&S₉₇ TB potential the lowest-energy interstitial minimum is a $\langle 110 \rangle$ -split interstitial, consistent with previous calculations,^{8,45,53} and that interstitials at tetrahedral sites or large extended arrangements are unfavorable. Our results indicate that the pathway with the lowest total activation energy is for vacancy migration, due to the low formation energy of this defect. We predict a two-step pathway for migration of $\langle 110 \rangle$ -split interstitials through the crystal by a combination of translational and rotational motions, mediated by true transition states rather than higher index saddle points. The relative activation energies for the migration of interstitial and vacancy defects suggest that vacancy diffusion will dominate at low temperatures and interstitial atom diffusion by the two-step pathway will occur at higher temperatures. These predictions are, of course, all dependent upon the quality of the TB potential that we have employed.

We have also run calculations to study the recombination of interstitial atoms with vacancies at first-, second- and third-nearest-neighbor positions. Each of the pathways shows the rotation of a split interstitial arrangement about a vacancy. However, calculations have only been completed on defect configurations using a 64-atom cell. Further work using a larger supercell is in progress to confirm the validity of these results.

ACKNOWLEDGMENTS

D.J.W. and L.J.M. are grateful to the Royal Society and the EPSRC for financial support, respectively.

-
- ¹P. M. Fahey, P. B. Griffin, and J. D. Plummer, *Rev. Mod. Phys.* **61**, 289 (1989).
- ²A. E. Michel, W. Rausch, P. A. Ronsheim, and R. H. Kastl, *Appl. Phys. Lett.* **50**, 416 (1987).
- ³G. D. Watkins, J. R. Troxell, and A. P. Chatterjee, in *Defects and Radiation Effects in Semiconductors*, edited by J. H. Albany, IOP Conf. Proc. No. 46 (Institute of Physics, Bristol, 1978), p. 16.
- ⁴G. D. Watkins, in *Materials Science and Technology*, edited by R. W. Cahn, P. Haasen, and E. J. Kramer (VCH, Weinheim, 1991), Vol. 4.
- ⁵Y. Bar-Yam and J. D. Joannopoulos, *Phys. Rev. Lett.* **52**, 1129 (1984).
- ⁶R. Car, P. J. Kelly, A. Oshiyama, and S. T. Pantelides, *Phys. Rev. Lett.* **52**, 1814 (1984).
- ⁷K. C. Pandey, *Phys. Rev. Lett.* **57**, 2287 (1986).
- ⁸S. J. Clark and G. J. Ackland, *Phys. Rev. B* **56**, 47 (1997).
- ⁹H. R. Schober, *Phys. Rev. B* **39**, 13 013 (1989).
- ¹⁰D. Maroudas and R. A. Brown, *Appl. Phys. Lett.* **62**, 172 (1993).
- ¹¹M. Nastar, V. V. Bulatov, and S. Yip, *Phys. Rev. B* **53**, 13 521 (1996).
- ¹²E. G. Song, E. Kim, Y. H. Lee, and Y. G. Hwang, *Phys. Rev. B* **48**, 1486 (1993).
- ¹³I. P. Batra, F. F. Abraham, and S. Ciraci, *Phys. Rev. B* **35**, 9552 (1987).
- ¹⁴J. Q. Broughton and X. P. Li, *Phys. Rev. B* **35**, 9120 (1987).
- ¹⁵R. Virkkunen, K. Laasonen, and R. M. Nieminen, *J. Phys.: Condens. Matter* **3**, 7455 (1991).
- ¹⁶J. F. Justo, M. Bazant, E. Kaxiras, V. Bulatov, and S. Yip, *Phys. Rev. B* **58**, 2539 (1998).
- ¹⁷C. Z. Wang, C. T. Chan, and K. M. Ho, *Phys. Rev. Lett.* **66**, 189 (1991).
- ¹⁸T. J. Lenosky, J. D. Kress, I. Kwon, A. F. Voter, B. Edwards, D. F. Richards, S. Yang, and J. B. Adams, *Phys. Rev. B* **55**, 1528 (1997).
- ¹⁹M. J. Puska, S. Poykko, M. Pesola, and R. M. Nieminen, *Phys. Rev. B* **58**, 1318 (1998).
- ²⁰J. Pancíř, *Collect. Czech. Chem. Commun.* **40**, 1112 (1975).
- ²¹C. J. Cerjan and W. H. Miller, *J. Chem. Phys.* **75**, 2800 (1981).
- ²²J. Simons, P. Jørgenson, H. Taylor, and J. Ozment, *J. Phys. Chem.* **87**, 2745 (1983).
- ²³D. O'Neal, H. Taylor, and J. Simons, *J. Phys. Chem.* **88**, 1510 (1984).
- ²⁴A. Banerjee, N. Adams, J. Simons, and R. Shepard, *J. Phys. Chem.* **89**, 52 (1985).
- ²⁵J. Baker, *J. Comput. Chem.* **7**, 385 (1986).

- ²⁶J. Baker, *J. Comput. Chem.* **8**, 563 (1987).
- ²⁷M. Menon and K. R. Subbaswamy, *Phys. Rev. B* **55**, 9231 (1997).
- ²⁸D. J. Wales, *J. Chem. Phys.* **101**, 3750 (1994).
- ²⁹D. J. Wales and T. R. Walsh, *J. Chem. Phys.* **105**, 6957 (1996).
- ³⁰J. N. Murrell and K. J. Laidler, *Trans. Faraday Soc.* **64**, 371 (1968).
- ³¹F. S. Acton, *Numerical Methods That Work* (Mathematical Association of America, Washington, DC, 1990), p. 204.
- ³²W. H. Press, S. A. Teukolsky, W. T. Vetterling, and B. P. Flannery, *Numerical Recipes in FORTRAN*, 2nd ed. (Cambridge University Press, Cambridge, 1992).
- ³³J. Baker and W. J. Hehre, *J. Comput. Chem.* **12**, 606 (1991).
- ³⁴M. Page and J. W. McIver, *J. Chem. Phys.* **88**, 922 (1988).
- ³⁵A. F. Voter, *Phys. Rev. Lett.* **78**, 3908 (1997).
- ³⁶T. R. Walsh and D. J. Wales, *Z. Phys. D* **40**, 229 (1997).
- ³⁷M. P. Allen and D. J. Tildesley, *The Computer Simulation of Liquids* (Clarendon, Oxford, 1987), p. 28.
- ³⁸A. C. Mackay, *Acta Crystallogr.* **15**, 916 (1962).
- ³⁹P. M. Morse, *Phys. Rev.* **34**, 57 (1929).
- ⁴⁰A. P. Sutton and J. Chen, *Philos. Mag. Lett.* **61**, 139 (1990).
- ⁴¹M. W. Finnis and J. E. Sinclair, *Philos. Mag. A* **50**, 45 (1984).
- ⁴²D. Tománek and M. Schluter, *Phys. Rev. B* **36**, 1208 (1987).
- ⁴³D. J. Chadi, *J. Vac. Sci. Technol.* **16**, 1290 (1979).
- ⁴⁴F. H. Stillinger and T. A. Weber, *Phys. Rev. A* **28**, 2408 (1983).
- ⁴⁵D. J. Chadi, *Phys. Rev. B* **46**, 9400 (1992).
- ⁴⁶D. J. Wales, *J. Chem. Soc., Faraday Trans.* **88**, 653 (1992).
- ⁴⁷D. J. Wales, *J. Chem. Soc., Faraday Trans.* **89**, 1305 (1993).
- ⁴⁸J. Zhu, T. Diaz de la Rubia, L. H. Yang, C. Mailhot, and G. H. Gilmer, *Phys. Rev. B* **54**, 4741 (1996).
- ⁴⁹P. E. Blöchl, E. Smargiassi, R. Car, D. B. Laks, W. Andreoni, and S. T. Pantelides, *Phys. Rev. Lett.* **70**, 2435 (1993).
- ⁵⁰Animated versions of these pathways may be found on our website at <http://brian.ch.cam.ac.uk/~lindsey/silicon.html>
- ⁵¹S. J. Clark, J. Crain, and G. J. Ackland, *Phys. Rev. B* **55**, 14 059 (1997).
- ⁵²R. E. Leone and P. V. R. Schleyer, *Angew. Chem. Int. Ed. Engl.* **9**, 860 (1970).
- ⁵³M. Tang, L. Colombo, J. Zhu, and T. Diaz De La Rubia, *Phys. Rev. B* **55**, 14 279 (1997).
- ⁵⁴N. Bernstein and E. Kaxiras, *Phys. Rev. B* **56**, 10 488 (1997).